Vacancy-type defects introduced by mechanical polishing in ammonothermal GaN studied by a monoenergetic positron beam

Akira Uedono[1], Shoji Ishibashi[2], Kohei Shima[3], Shigefusa F. Chichibu[3], Kacper Sierakowski[4], Makoto Oishi[5], Noriyuki Okada[5], Takuro Nagai[5], and Michal Bockowski[4]

[1]*Institute of Pure and Applied Science, University of Tsukuba, Tsukuba, Ibaraki 305-8573, Japan*

[2]*Center for Computational Sciences, University of Tsukuba, Tsukuba, Ibaraki 305-8577, Japan*

[3]*Institute of Multidisciplinary Research for Advanced Materials, Tohoku University, Sendai 980-8577, Japan*

[4]*Institute of High Pressure Physics, Polish Academy of Sciences, Sokolowska 29/37, 01-142 Warsaw, Poland*

[5]*National Institute for Materials Science (NIMS), Tsukuba, Ibaraki 305-0044, Japan*

Vacancy-type defects introduced by mechanical polishing in basic ammonothermal GaN and their annealing behavior were studied using a monoenergetic positron beam. The major vacancy-type defect in the sample was identified as a Ga-vacancy (V_{Ga}) coupled with hydrogen atoms. After mechanical polishing, high-density dislocations and stacking faults were introduced in the subsurface region (< 240 nm). In this region, the vacancy-type defects detected by positron annihilation were divacancies ($V_{Ga}V_N$) and their complexes with hydrogen atoms. After ultra-high-pressure annealing at 1400ºC, {0001} basal slip bands were the predominant defects observed using a transmission

electron microscope. The major vacancy-type defects for the annealed samples were identified as V_{Ga} coupled with multiple V_N [ex $V_{Ga}(V_N)_3$] and their complexes with hydrogen atoms. The observed annealing behavior of vacancies agreed with that estimated using photoluminescence spectroscopy.

Keywords

Mechanical polishing; GaN; Vacancy; Defect; Positron annihilation

1. Introduction

Gallium nitride (GaN) is the primary widegap semiconductor for not only optoelectronic devices but also high-frequency and high-power devices [1–3]. With its high electron velocity, high breakdown strength, high thermal conductivity, and low on-resistance, GaN-based power devices have pushed forward the limits of Si- and SiC-based power chips. The application fields of GaN-based power devices will expand into next-generation networks as well as the automotive and aerospace industries. Most commercially available GaN-based devices have been fabricated using GaN grown on foreign substrates such as Si, SiC, GaAs, and sapphire, due to the difficulty in growing cost-effective GaN substrates. Thus, technologies have been extensively studied for suppressing the introduction of defects, such as threading dislocations, caused by lattice mismatch between GaN and substrates [2,4]. However, demand is increasing for free-standing GaN substrates for fabricating high-quality optical devices and vertical high-power transistors. The major growth techniques for bulk GaN are ammonothermal and sodium-flux methods [5–9]. The significant features of these GaN substrates are their low threading dislocation density (TDD) and low curvature radius [8,9]. GaN wafers grown by halide vapor phase epitaxy (HVPE) and its derivative, oxide vapor phase epitaxy (OVPE), are often used as "quasi-bulk" GaN substrates [10,11]. However, they have larger TDD and curvature radius than bulk GaN because of the differences in lattice constants and thermal expansion coefficients of GaN and foreign substrates.

In the ammonothermal growth technique, GaN feedstock is dissolved in supercritical ammonia in a high-pressure autoclave [6,8,9]. The dissolved feedstock is transported to native seeds, and the crystallization occurs under supersaturation conditions. To accelerate crystal growth, mineralizers are added to the ammonia, thereby enhancing the

dissociation and solubility of GaN. The typical growth temperature and pressure of ammonia are 400–750°C and 100–600 MPa. In the sodium-flux method, Ga and Na are mixed in a crucible at around 900ºC under a nitrogen atmosphere (0.5–5 MPa), where Na increases the solubility of atomic nitrogen in the Ga flux [5,7].

After crystal growth, wafers are fabricated through multiple procedures, including wire saw cutting, mechanical polishing (grinding and lapping), and chemical-mechanical polishing (CMP) [12–16]. GaN crystals, however, exhibit high brittleness and hardness but low fracture toughness, which easily leads to brittle damage, such as fractures and cracks, during machining [14,16]. The major phenomena during mechanical polishing are plastic deformation and lattice distortions at elevated temperatures due to grinding heat, which introduce high-density stacking faults, dislocations, amorphous regions, and nanocrystalline regions. These types of damage are removed by post-grinding processes such as lapping and CMP. To fabricate an epitaxial-ready surface, the root-mean-square (RMS) roughness must be less than 0.1 nm [8]. Because the removal rate of CMP is low, wafering time is governed by this process, and hence affects the overall manufacturing cost. Both mechanical and chemical processes during the wafering process are closely related to the final surface conditions [15,17]. Thus, defects introduced by the mechanical polishing process need to be known in detail to optimize wafering process parameters. Positron annihilation is a technique for characterizing vacancy-type defects in solid-state materials [18]. This technique has been used to detect vacancy-type defects in bulk GaN and GaN grown on foreign substrates [19–23]. In the present study, we used a monoenergetic positron beam to characterize vacancy-type defects introduced by the mechanical polishing process in basic ammonothermal GaN.

2. Experimental

The samples investigated were 1-in.-diameter GaN wafers grown by using the basic ammonothermal process on native substrates. Details of the growth method, reactor configurations, and the physical properties of basic ammonothermal GaN are described elsewhere [8,9,24]. The major impurities in the samples were hydrogen (10^{19} cm^{-3}) and oxygen (10^{19} cm^{-3}). The samples with two types of (0001) surface preparation were studied. The first type will be referred to as "rough polishing," and the second one as "optically flat." Details about both surface finishes were given in Table 1. The samples were first cut from bulk as-grown crystal using a wire saw and then lapped on both sides (N-polar and Ga-polar). The rough-polished sample underwent polishing step 1, and the optically flat sample underwent all the polishing steps. The two presented surface finishes are representing wafering steps preceding CMP. More details about the wafering procedure can be found elsewhere [25]. To understand the annealing behavior of defects introduced by the rough polishing, the samples were annealed at temperatures between 1000°C and 1400°C for 5 min under a N_2 pressure of 1 GPa using an ultra-high-pressure annealing (UHPA) system [26].

The surface conditions of the samples before annealing were characterized using an X-ray diffractometer (XRD). From measurements of 2θ-ω XRD profiles for the sample after rough polishing, the full-widths-at-half-maximum (FWHMs) of the reflection from (002) were found to be 161 and 146 arcsec along the *a*- and *m*-axes, respectively. After optically flat polishing, they decreased to 28 and 36 arcsec, respectively. The surface morphologies for the samples after rough and optical polishings were evaluated using atomic force microscopy (AFM). Figure 1 shows AFM images of these samples, where RMS after rough and optical polishings were 8.7 nm and 0.17 nm, respectively. The

damaged subsurface of the rough-polished sample was also characterized using a transmission electron microscope (TEM). The sample was prepared by focused ion beam (FIB) milling (Ethos NX5000 series, Hitachi High-Tech Co.) after covering the surface with carbon layers. TEM bright-field (BF) images were obtained by the Thermo Fisher Scientific Talos F200X G2 transmission electron microscope. Photoluminescence (PL) spectra were measured by using a He-Cd laser at 325 nm and a power density of 38 W/cm^2 at room temperature.

Details of the positron annihilation spectroscopy and its application for the characterization of vacancy-type defects are described elsewhere [18,22,23,27]. A monoenergetic positron beam was used to measure Doppler broadening spectra of the annihilation radiation as a function of incident positron energy E. Obtained spectra were characterized by the S parameter defined as the fraction of annihilation events in the energy range between 510.22 and 511.78 keV, and by the W parameter defined as the number of annihilation events in the energy ranges of 504.14–507.96 and 514.04–517.86 keV. The depth distributions of vacancy-type defects in the rough-polished samples before and after annealing were obtained by analyzing the S–E relationship using the computer code VEPFIT [28]. The coincidence Doppler broadening technique was also used to identify the vacancy-type defects in the samples [18].

The Doppler broadening spectra for the positron annihilation in GaN containing vacancy-type defects and defect-free (DF) GaN were simulated by QMAS (Quantum MAterials Simulator) code [29,30]. Details on the simulation of positron annihilation in group-III nitrides using QMAS are given elsewhere [31,32]. The simulation code uses the projector augmented-wave (PAW) method [33] and a plane-wave basis set. An orthorhombic supercell equivalent to 4 × 4 × 2 hexagonal unit cells with a wurtzite

structure was used in the calculation. The number of atoms in the supercell was 128 if there is no vacancy. The planewave energy cutoff and the force convergence criterion were set to be 20 Ha and 5×10^{-5} Ha/Bohr, respectively. Only the Γ point is used for the Brillouin zone sampling. Atomic positions were optimized by determining the Hellmann-Feynman forces, where the effect of a positron on the atomic configurations was not considered. The electronic exchange-correlation interaction was treated on the basis of the Perdew–Burke–Ernzerhof-type generalized gradient approximation [34]. The electron-positron interaction was treated on the basis of the local-density approximation [35]. The energy resolution of the Ge detectors for coincidence Doppler broadening spectra (0.90 keV, full width at half maximum) was convoluted with the simulated spectra.

3. Results and Discussion

Figure 2 shows cross-sectional BF-TEM images of the samples after (a) rough polishing and annealing at (b) 1000ºC, (c) 1100ºC, (d) 1200ºC, and (e) 1400ºC. Before annealing treatment [Fig. 2(a)], the observed surface morphology is typical for GaN wafers after mechanical polishing [14–16]. In the subsurface region (< 100 nm), the dark area corresponds to the region with high-density stacking faults and dislocations. The area is also expected to include amorphous regions resulting from lattice distortions induced by abrasive stress [16,36,37]. The arrows in Fig. 2(a) show dislocations along with pyramidal planes, which are also typical defects introduced by mechanical polishing [16] and deformation by Vickers indentation [38–40]. In the region > 100 nm, dislocation loops multiply and move by cross-slips on the {0001} basal and $\{10\bar{1}1\}$ pyramidal planes [38].

Above 1100ºC annealing [Fig. 2(c)–(e)], the dark area (< 100 nm) and the

dislocations along the pyramidal planes disappeared and were replaced by {0001} basal slip bands [arrows in Fig 2(e)]. These slip bands are also common defects introduced by the Vickers hardness test [38–40]. The basal slip band is a more stable defect than non-basal slip systems in hcp materials. At high annealing temperatures (> 1100°C), a certain amount of stress can be introduced by the recrystallization of the subsurface amorphous region. The basal slip band is considered to effectively suppress such stress. Horibuchi *et al*. [41] reported that threading dislocations in basic ammonothermal GaN were changed into helical dislocations while the epitaxial layer was being deposited on the GaN substrate at 1100°C. The helical dislocations mainly consisted of dislocations along the {0001} basal planes, suggesting that basal-plane defects are stable at high temperature.

Figure 3 shows the *S* values of rough-polished GaN before and after annealing (1000, 1100, 1200, 1400°C) as a function of *E*. The mean positron implantation depth is shown on the upper horizontal axis. The *S*–*E* relationship for optical-polished GaN is also shown. For this sample, the *S* value saturated at $E > 10$ keV, suggesting that the positron annihilation at the surface had a negligible effect in this energy range, and the obtained *S* value is the one corresponding to the positron annihilation in bulk. The *S* value for defect-free GaN is reported to be 0.442 [22,23,27]. The larger *S* value (0.451) for ammonothermal GaN, therefore, is due to the trapping of positrons by vacancies. The diffusion length of positrons (L_d) for optical-polished GaN was obtained to be 30±2 nm. This value is shorter than typical defect-free GaN (80-100 nm) [22,23], suggesting the suppression of the positron diffusion due to vacancies. After rough polishing, the *S* value in the subsurface region ($E < 10$ keV) increased, suggesting the trapping of positrons by vacancy-type defects. The *S* value in the damaged region increased after 1000°C and began to decrease above 1100°C.

By analyzing the *S*–*E* relationships, the depth distributions of *S* were obtained. In the fitting procedure, the region scanned by positrons was divided into three blocks, with the 3rd (deepest) block corresponding to the bulk *S* value. The fitting determined the *S* values for each block and their positions. For rough-polished GaN, L_d in the 3rd block was fixed to that of optical-polished GaN. The L_d values in the first block were determined from the fits and were obtained to be about 10 nm. The value of L_d in the 2nd block was fixed to be the one for the 1st block. The solid curves in Fig. 3 are fits to the experimental data, and Fig. 4 shows the obtained depth distribution of *S*. Before annealing, the high *S* value (0.477) was observed in the subsurface region (< 50 nm) and remained at 0.47 up to 240 nm. The observed behavior of *S* reasonably agreed with the surface morphology observed by TEM (Fig. 2). After annealing at 1000°C, the *S* value at < 50 nm increased, which can be attributed to vacancy-type defects agglomerating in the highly damaged area. After annealing above 1100°C, the *S* value in this region tended to decrease preferentially.

The species of vacancy-type defects can be identified by using the relationship between the *S* and *W* parameters [18]. Figure 5 shows *S*–*W* plots obtained from the coincidence Doppler broadening spectra for the rough-polished GaN samples before and after annealing (brown symbols). As shown in Fig. 3, the region that yields a high *S* value shifted toward the inside of the sample as the annealing temperature increased. To evaluate these regions, the *E* values for the coincidence measurement increased with annealing temperature. For the sample before annealing, *E* was fixed at 2.1 keV. The values of *E* were fixed at 3.6, 5.6, 6.6, and 6.6 keV for the samples annealed at 1000°C, 1100°C, 1200°C, and 1400°C, respectively. The (*S*,*W*) values for the ammonothermal GaN after optical polishing and defect-free GaN grown by using metal-organic vapor phase epitaxy (MOVPE) on the GaN substrate were also measured at *E* = 28.6 keV. The

latter value corresponds to the positron annihilation in defect-free (DF) GaN [42]. The simulated (S,W) values for defect-free GaN ($DF_{(cal)}$), a Ga-vacancy V_{Ga}, their complexes with nitrogen vacancy (V_N) [$V_{Ga}(V_N)_n$, n=1–3], and these complexes with oxygen and hydrogen [$V_{Ga}(O_N)_n$, nH-V_{Ga}, and H-$V_{Ga}(V_N)_n$, n=1–4] are also shown in Fig. 5 (blue symbols).

For the sample after optical polishing, the (S,W) value was close to that of 2H-V_{Ga}. For ammonothermal GaN prepared under similar growth conditions to those used in the present experiment, the (S,W) value was obtained to be almost identical to that of optical-polished GaN [23]. In this report (ref. 23), the positron lifetime spectrum was also measured and analyzed assuming a single component, with a positron lifetime of 0.181 ns. This lifetime was longer than the positron lifetime for typical defect-free GaN (0.16 ns) [22], suggesting that almost all positrons annihilate from the trapped state. The simulated positron lifetime for 2H-V_{Ga} was reported to be 0.185 ns [23], which was close to the obtained lifetime for the ammonothermal GaN. Thus, the major defects in optical-polished GaN can be identified as V_{Ga} coupled with hydrogen atoms. This is consistent with previous reports on basic and acidic ammonothermal GaN [20,21,43]. For the sample after rough polishing, the (S,W) value was close to that of $V_{Ga}V_N$ and/or H-$V_{Ga}V_N$, suggesting that the major vacancy-type defects detected by positron annihilation in the deformed region are such defects. After annealing at 1000°C, the value shifted to the upper-right. Above 1100°C, the values appear to lie on a line, but an extension of the line toward the left-hand side does not approach the defect-free value. This suggests that the observed variation of the (S,W) values was not due to vacancy concentration decreasing but to the defect species changing. Because the value for the sample after annealing at 1400°C was close to the (S,W) for H-$V_{Ga}(V_N)_3$, the average number of hydrogen atoms

trapped by vacancy clusters [ex $V_{Ga}(V_N)_3$] increased as temperature increased from 1000°C to 1400°C. For ion-implanted GaN (before annealing), the major defect species was reported to be V_{Ga}-type defects (V_{Ga} and/or $V_{Ga}V_N$) [27,42,44]. If the vacancy concentration is high, the defect size increases to $(V_{Ga}V_N)_3$ after annealing at 1000°C [27,44]. Because the motion of dislocations consumes vacancies, the suppression of the increase in vacancy clusters in the present samples could result from high-density dislocations as a sink of vacancies. The formation energies (E_F) of complexes of V_{Ga}-type defects and hydrogen atoms in GaN have been calculated using first-principles density-functional theory [45–48]. The value of E_F depends on the Fermi level position, but E_F for *n*H-V_{Ga} tends to be lower than E_F for V_{Ga}, and the same is true for larger vacancies such as $V_{Ga}V_N$. The energy required for removing hydrogen atoms from a hydrogenated vacancy is positive. Thus, the formation of vacancy-hydrogen complexes could also account for the suppression of larger vacancy clusters after high-temperature annealing. In Fig. 4, the *S* value in the subsurface region (30–60 nm) decreased after annealing above 1100°C. During UHPA, hydrogen was reported to be introduced from the atmosphere during annealing above 1000°C [27]. Thus, the decrease in *S* in this region can be attributed to the formation of vacancy complexes with hydrogen atoms diffused from the surface.

Figure 6 shows PL intensities for GaN wafers after rough polishing and annealing treatments (1000–1400ºC). The result for the sample after optical polishing is also shown. For this sample, the origin of the green luminescence (GL) band (2.40 eV) has been attributed to several causes, including nitrogen vacancy (V_N)-related defects and a carbon atom at the nitrogen site (C_N) [49–51]. Because the carbon concentration in ammonothermal GaN is relatively low, the origin of the GL band can be attributed to V_N-

related defects [52,53]. The blue luminescence (BL) at 2.96 eV has also been attributed to several defects, such as Mg_{Ga}, Zn_{Ga}, C_N, C_{Ga}, and V_{Ga}-related complexes [54–59]. For ammonothermal GaN, the most probable candidate was reported to be V_{Ga} coupled with hydrogen and/or oxygen atoms [52], but Mg_{Ga} and/or Zn_{Ga} could be partially associated with this luminescence peak [57].

The intensities of near-band-edge (NBE) emission, GL, and BL emissions decreased due to non-radiative recombination centers being introduced by rough polishing. After annealing at 1000°C and 1100°C, the intensities of these emission bands recovered as annealing temperature increased. After annealing at 1200°C, however, the GL band intensity began to decrease, and the BL emission became the dominant contributor to the luminescence after annealing at 1400°C. As discussed above, the annealing of the rough-polished sample increases the number of V_N coupled with V_{Ga}-type defects. Thus, the observed suppression of the GL band can be attributed to complexes forming between V_{Ga}-type defects and to the concentration of V_N-type defects decreasing.

4. Summary

We used positron annihilation to study vacancy-type defects introduced by rough polishing in basic ammonothermal GaN. Doppler broadening spectra of the annihilation radiation were measured for the samples before and after the polishing. The major vacancy-type defect in the sample was identified as V_{Ga}-type defects coupled with hydrogen atoms. The rough polishing introduced high-density stacking faults and dislocations in the subsurface region (< 240 nm). The major vacancy-type defects in this region were divacancies and their hydrogen-complexed forms. After UHPA at 1400 °C, {0001} basal slip bands were the predominant defects observed by using a TEM. Even at

this temperature, high-density vacancy-type defects were still found to exist, and the number of V_N coupled with V_{Ga} increased (ex. H-$V_{Ga}V_N \rightarrow$ H-$V_{Ga}(V_N)_3$). The variation of PL spectra for the samples before and after annealing was well explained by the annealing behavior of vacancies observed by positron annihilation. The present work showed that positron annihilation spectroscopy is a valuable technique for optimizing both mechanical and chemical polishing processes, because it can determine depth distributions of defects and the defect species non-destructively.

Acknowledgements

This work was performed under the Cooperative Research Program of "Network Joint Research Center for Materials and Devices (MEXT)". The part of this work has been supported by the Wide Bandgap (WBG) Pilot line, which is funded jointly by the Chips Joint Undertaking, through the European Union's Digital Europe programme and Horizon Europe programme, as well as by the participating states Italy, Sweden, Poland, Finland, Austria, France, and Germany, under Grant Agreement n. 101183211. This work was also supported in part by MEXT Promotion of Development of a Joint Usage / Research System Project: Coalition of Universities for Research Excellence Program (CURE) (Grant Number JPMXP1323015474). Numerical calculations were performed (in part) using the supercomputer ''Flow'' at the Information Technology Center, Nagoya University. A part of this work was supported by "Advanced Research Infrastructure for Materials and Nanotechnology in Japan (ARIM)" of MEXT (Proposal Number JPMXP1223NM0137).

1. M. H. Crawford, IEEE J Selected Topics in Quantum Electronics 15 (2009) 1028–1040. https://doi.org/10.1109/jstqe.2009.2013476.
2. S. J. Pearton, F. Ren, A. P. Zhang, K. P. Lee, Mat. Sci. Eng. R30 (2000) 55–212. https://doi.org/10.1016/S0927-796X(00)00028-0.
3. J. P. Kozak, R. Zhang, M. Porter, Q. Song, J. Liu, B. Wang, R. Wang, W. Saito, Y. Zhang, Stability, IEEE Trans. Power Electronics 38 (2023) 8442–8471. https://doi.org/10.1109/tpel.2023.3266365.
4. Y. Zhong, J. Zhang, S. Wu, L. Jia, X. Yang, Y. Liu, Y. Zhang, Q. Sun, Fundam. Res. 2 (2022) 462–475. https://doi.org/10.1016/j.fmre.2021.11.028.
5. Y. Mori, M. Imanishi, K. Murakami, M. Yoshimura, Jpn. J. Appl. Phys. 58 (2019) SC0803. https://doi.org/10.7567/1347-4065/ab112e.
6. D. Tomida, Q. Bao, M. Saito, K. Kurimoto, F. Sato, T. Ishiguro, S. F. Chichibu, Appl. Phys. Exp. 11 (2018) 091002. https://doi.org/10.7567/apex.11.091002.
7. M. Imanishi, K. Murakami, T. Yamada, K. Kakinouchi, K. Nakamura, T. Kitamura, K. Okumura, M. Yoshimura, Y. Mori, Appl. Phys. Exp. 12 (2019) 045508. https://doi.org/10.7567/1882-0786/ab0db6.
8. R. Kucharski, T. Sochacki, B. Lucznik, M. Bockowski, J. Appl. Phys. 128 (2020) 050902. https://doi.org/10.1063/5.0009900.
9. M. Bockowski, I. Grzegory, Acta. Phys. Polonica A 141 (2022) 167–174. https://doi.org/10.12693/APhysPolA.141.167.
10. D. Nakamura, T. Kimura, Appl. Phys. Exp. 11 (2018) 065502. https://doi.org/10.7567/APEX.11.065502.
11. S. Usami, A. Shimizu, R. Higashiyama, M. Imanishi, J. Takino, T. Sumi, Y. Okayama, M. Maruyama, M. Yoshimura, M. Hata, M. Isemura, Y. Mori, Jpn. J. Appl.

Phys. 64 (2025) 055504. https://doi.org/10.35848/1347-4065/adce8c.

12. J. Sun, P. Chen, F. Qin, T. An, H. Yu, B. He, Precision Eng. 51 (2018) 625–637. https://doi.org/10.1016/j.precisioneng.2017.11.003.
13. A. Haapalinna, S. Nevas, D. Pähler, Mat. Sci. Eng. 107 (2004) 321–331. https://doi.org/10.1016/j.mseb.2003.12.008.
14. H. Aida, H. Takeda, T. Doi, Precision Eng. 67 (2021) 67:350–358. https://doi.org/10.1016/j.precisioneng.2020.10.007.
15. C. Li, Y. Piao, B. Meng, Y. Hu, L. Li, F. Zhang, Int. J. Machine Tools & Manuf. 172 (2022) 103827. https://doi.org/10.1016/j.ijmachtools.2021.103827.
16. C. Li, Y. Hu, Z. Wei, C. Wu, Y. Peng, F. Zhang, Y. Geng, J. Extrem. Manuf. 6 (2024) 025103. https://doi.org/10.1088/2631-7990/ad207f.
17. S. Gao, H. Li, H. Huang, R. Kang, Appl. Surf. Sci. 599 (2022) 153982. https://doi.org/10.1016/j.apsusc.2022.153982.
18. F. Tuomisto, I. Makkonen, Rev. Mod. Phys. 85 (2013) 1583–1631. https://doi.org/10.1103/RevModPhys.85.1583.
19. K. Saarinen, T. Suski, I. Grzegory, D. C. Look, Phys. Rev. B 64 (2001) 233201. https://doi.org/10.1103/PhysRevB.64.233201.
20. F. Tuomisto, K. Saarinen, B. Lucznik, I. Grzegory, H. Teisseyre, T. Suski, S. Porowski, P. R. Hageman, J. Likonen, Appl. Phys. Lett. 86 (2005) 031915. https://doi.org/10.1063/1.1854745.
21. S. Suihkonen, S. Pimputkar, S. Sintonen, F. Tuomisto, Adv. Electron. Mater. 3 (2017) 1600496. https://doi.org/10.1002/aelm.201600496.
22. A. Uedono, M. Imanishi, M. Imade, M. Yoshimura, S. Ishibashi, M. Sumiya, Y. Mori, J. Cryst. Growth 475 (2017) 261–265. https://doi.org/10.1016/j.jcrysgro.2017.06.027

23. A. Uedono, J. Takino, T. Sumi, Y. Okayama, M. Imanishi, S. Ishibashi, Y. Mori, J. Cryst. Growth 570 (2021) 126219. https://doi.org/10.1016/j.jcrysgro.2021.126219.
24. M. Zajac, R. Kucharski, K. Grabianska, A. Gwardys-Bak, A. Puchalski, D. Wasik, E. Litwin-Staszewska, R. Piotrzkowski, J. Z. Domagala, M. Bockowski, Progress in Crystal Growth & Characterization of Mater. 64 (2018) 63–74. https://doi.org/10.1016/j.pcrysgrow.2018.05.001.
25. T. Sochacki, L. Kirste, R. Kucharski, M. Iwinska, Y. Kumagai, M. Bockowski, 2.03 - Growth of bulk GaN crystals for the production of substrates, in Comprehensive Semiconductor Science and Technology (2nd ed.), Elsevier B. V., 2025. p. 71–105. https://doi.org/10.1016/B978-0-323-96027-4.00030-9.
26. K. Sierakowski, R. Jakiela, B. Lucznik, P. Kwiatkowski, M. Iwinska, M. Turek, H. Sakurai, T. Kachi, M. Bockowski, Electronics 9 (2020) 1380. https://doi.org/10.3390/electronics9091380.
27. A. Uedono, H. Sakurai, T. Narita, K. Sierakowski, M. Bockowski, J. Suda, S. Ishibashi, S. F. Chichibu, T. Kachi, Sci. Rep. 10 (2020) 17349. https://doi.org/10.1038/s41598-020-74362-9.
28. A. Van Veen, H. Schut, M. Clement, J. M. M. Nijs, A. Kruseman, M. R. IJpma, Appl. Surf. Sci. 85 (1995) 216–224. https://doi.org/10.1016/0169-4332(94)00334-3.
29. S. Ishibashi, T. Tamura, S. Tanaka, M. Kohyama, K. Terakura, Phys. Rev. B 76 (2007) 153310. https://doi.org/10.1103/PhysRevB.76.153310.
30. S. Hagiwara, S. Ishibashi, M. Otani, Phys. Rev. B 110 (2024) 155409. https://doi.org/10.1103/PhysRevB.110.155409.
31. S. Ishibashi, A. Uedono, J. Phys. Conf. Ser. 505 (2014) 012010. https://doi.org/10.1088/1742-6596/505/1/012010.

32. S. Ishibashi, A. Uedono, H. Kino, T. Miyake, K. Terakura, J. Phys. Cond. Matter 31 (2019) 475401. https://doi.org/10.1088/1361-648X/ab35a4.
33. P. E. Blöchl, Phys. Rev. B. 50 (1994) 17953–17979. https://doi.org/10.1103/physrevb.50.17953.
34. J. P. Perdew, K. Burke, M. Ernzerhof, Phys. Rev. Lett. 17 (1996) 3865–3868. https://doi.org/10.1103/PhysRevLett.77.3865.
35. E. Boroński, R. M. Nieminen, Phys. Rev. B 34 (1986) 3820–3831. https://doi.org/10.1103/physrevb.34.3820.
36. V.-T. Nguyen, T.-H. Fang, Thin Solid Films 731 (2021) 138744. https://doi.org/10.1016/j.tsf.2021.138744.
37. C. Jing, H. Dai, Mater. Sci. Semiconductor Processing 185 (2025) 108951. https://doi.org/10.1016/j.mssp.2024.108951.
38. J. Huang, K. Xu, X. J. Gong, J. F. Wang, Y. M. Fan, J. Q. Liu, X. H. Zeng, G. Q. Ren, T. F. Zhou, H. Yang, Appl. Phys. Lett. 98 (2011) 221906. https://doi.org/10.1063/1.3593381.
39. M. Fujikane, T. Yokogawa, S. Nagao, R. Nowak, Jpn. J. Appl. Phys. 52 (2013) 08JJ01. https://doi.org/10.7567/jjap.52.08jj01.
40. Y. Ishikawa, Y. Sugawara, D. Yokoe, Y. Yao, Jpn. J. Appl. Phys. 59 (2020) 091005. https://doi.org/10.35848/1347-4065/abb00c.
41. K. Horibuchi, S. Yamaguchi, Y. Kimoto, K. Nishikawa, T. Kachi, Semicond. Sci. Technol. 31 (2016) 03400. https://doi.org/10.1088/0268-1242/31 /3/034002.
42. A. Uedono, H. Iguchi, M. Horita, J. Suda, K. Shima, S. F. Chichibu, S. Ishibashi, Phys. Stat. Sol. (b) (2025) e202500409. https://doi.org/10.1002/pssb.202500409.
43. A. Uedono, Y. Tsukada, Y. Mikawa, T. Mochizuki, H. Fujisawa, H. Ikeda, K.

Kurihara, K. Fujito, S. Terada, S. Ishibashi, S. F. Chichibu, J. Cryst. Growth 448 (2016) 117–121. https://doi.org/10.1016/j.jcrysgro.2016.05.015.

44. A. Uedono, H. Sakurai, J. Uzuhashi, T. Narita, K. Sierakowski, S. Ishibashi, S. F. Chichibu, M. Bockowski, J. Suda, T. Ohkubo, N. Ikarashi, K. Hono, T. Kachi, Phys. Stat. Sol. (b) 259 (2022) 2200183. https://doi.org/10.1002/pssb.202200183.
45. C. Van de Walle, Phys. Rev. B 56 (1997) R10020. https://doi.org/10.1103/PhysRevB.56.R10020.
46. C. Van de Walle, J. Neugebauer, J. Appl. Phys. 95 (2004) 3851–3879. https://doi.org/10.1063/1.1682673.
47. A. F. Wright, J. Appl. Phys. 90 (2001) 1164–1168. https://doi.org/10.1063/1.1383980.
48. Y. S. Puzyrev, T. Roy, M. Beck, B. R. Tuttle, R. D. Schrimpf, D. M. Fleetwood, S. T. Pantelides, J. Appl. Phys. 109 (2011) 034501. https://doi.org/10.1063/1.3524185.
49. J. L. Lyons, A. Janotti, C. G. Van de Walle, Appl. Phys. Lett. 97 (2010) 152108. https://doi.org/10.1063/1.3492841.
50. T. Narita, K. Tomita, Y. Tokuda, T. Kogiso, M. Horita, T. Kachi, J. Appl. Phys. 124 (2018) 215701. https://doi.org/10.1063/1.505737.
51. M. A. Reshchikov, D. O. Demchenko, J. D. McNamara, S. Fernández-Garrido, R. Calarco, Phys. Rev. B 90 (2014) 035207. https://doi.org/10.1103/PhysRevB.90.035207.
52. K. Shima, K. Kurimoto, Q. Bao, Y. Mikawa, M. Saito, D. Tomida, A. Uedono, S. Ishibashi, T. Ishiguro, S. F. Chichibu SF, Appl. Phys. Lett. 124 (2024) 181103. https://doi.org/10.1063/5.0208853.
53. S. F. Chichibu, K. Shima, A. Uedono, S. Ishibashi, H. Iguchi, T. Narita, K. Kataoka,

R. Tanaka, S. Takashima, K. Ueno, M. Edo, H. Watanabe, A. Tanaka, Y. Honda, J. Suda, H. Amano, T. Kachi, T. Nabatame, Y. Irokawa, Y. Koide, J. Appl. Phys. 135 (2024) 185701. https://doi.org/10.1063/5.0201931.

54. H. Alves, M. Bohm, A. Hofstaetter, H. Amano, S. Einfeldt, D. Hommel, D. M. Hofmann, B. K. Meyer, Physica B 308 (2001) 38–41. https://doi.org/10.1016/S0921-4526(01)00663-9.
55. M. A. Reshchikov, J. Appl. Phys. 129 (2021) 121101. https://doi.org/10.1063/5.0041608.
56. R. Armitage, Q. Yang, E. R. Weber, J. Appl. Phys. 97 (2005) 073524. https://doi.org/10.1063/1.1856224.
57. M. A. Reshchikov, Solids 6 (2025) 52. https://doi.org/10.3390/solids6030052.
58. M. Toth, K. Fleischer, M. R. Phillips, Phys. Rev. B 59 (1999) 1575–1578. https://doi.org/10.1103/PhysRevB.59.1575.
59. H. C. Yang, T. Y. Lin, Y. F. Chen, Phys. Rev. B 62 (2000) 12593–12596. https://doi.org/10.1103/PhysRevB.62.12593.

Fig. 1. AFM images of basic ammonothermal GaN wafers after (a) rough polishing (RMS = 8.7 nm) and (b) optical polishing (RMS = 0.17 nm).

Fig. 2. Cross-sectional BF-TEM images of basic ammonothermal GaN wafers after (a) rough polishing and annealing at (b) 1000°C, (c) 1100°C, (d) 1200°C, and (e) 1400°C.

Fig. 3. *S* parameters as a function of incident positron energy *E* for ammonothermal GaN wafers after rough polishing and annealing treatments (1000–1400°C). Results for the wafer after CMP are also shown. Solid curves represent fits to experimental data, and results are shown in Fig. 3. Ranges of green, blue, and ultraviolet luminescence bands (GL, BL, and UVL) are shown.

Fig. 4. Depth distributions of *S* for ammonothermal GaN wafers after rough polishing and annealing treatments (1000–1400°C).

Fig. 5. *S*–*W* relationships for ammonothermal GaN wafers after rough polishing (RP) and annealing treatments (1000–1400°C). (*S*,*W*) values for ammonothermal GaN after optical polishing (OP) and MOVPE-GaN (DF) are also shown. (*S*,*W*) obtained by simulations for defect-free GaN ($DF_{(cal)}$), V_{Ga}, $V_{Ga}(V_N)_n$, $V_{Ga}(O_N)_n$, *n*H-V_{Ga}, H-$V_{Ga}(V_N)_n$ (n = 1–4) are shown as blue symbols.

Fig. 6. PL intensities for ammonothermal GaN wafers after rough polishing (RP) and annealing treatments (1000–1400°C). The result for the wafer after optical polishing (OP) is also shown. Energy ranges corresponding to red, yellow, green, blue, and

ultraviolet luminescence are shown as bars (RL, YL, GL, BL, and UVL).

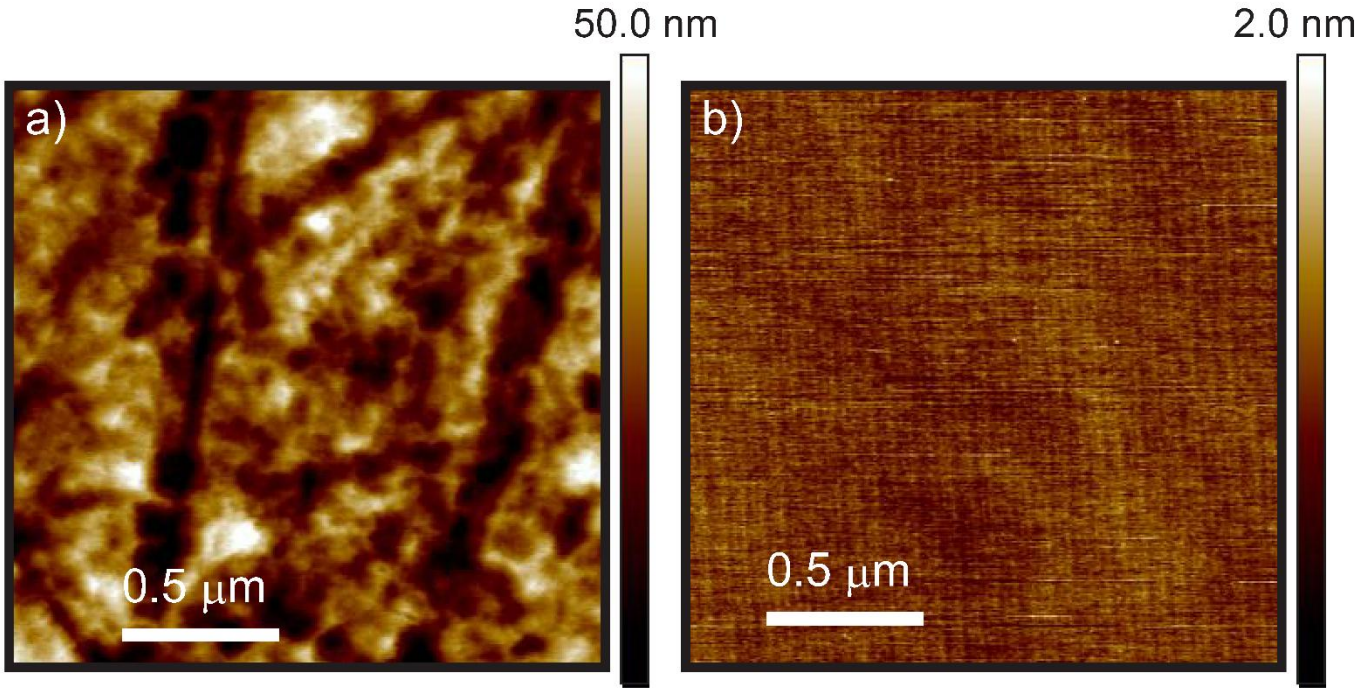

Fig. 1

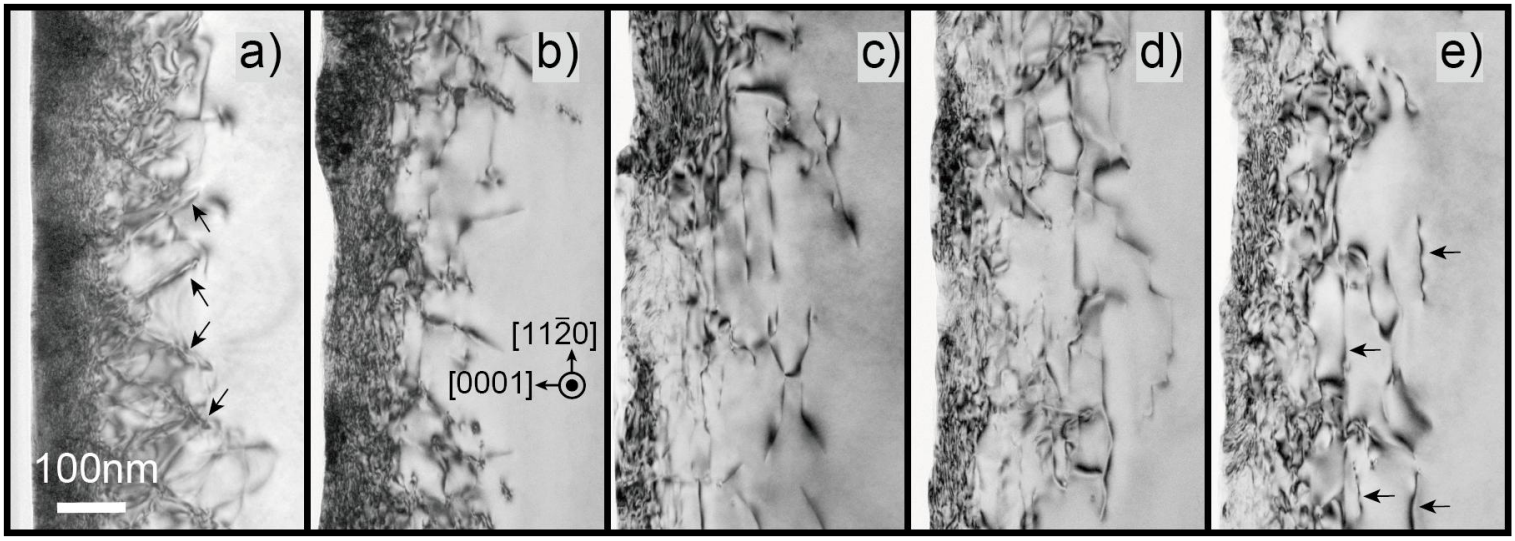

Fig. 2

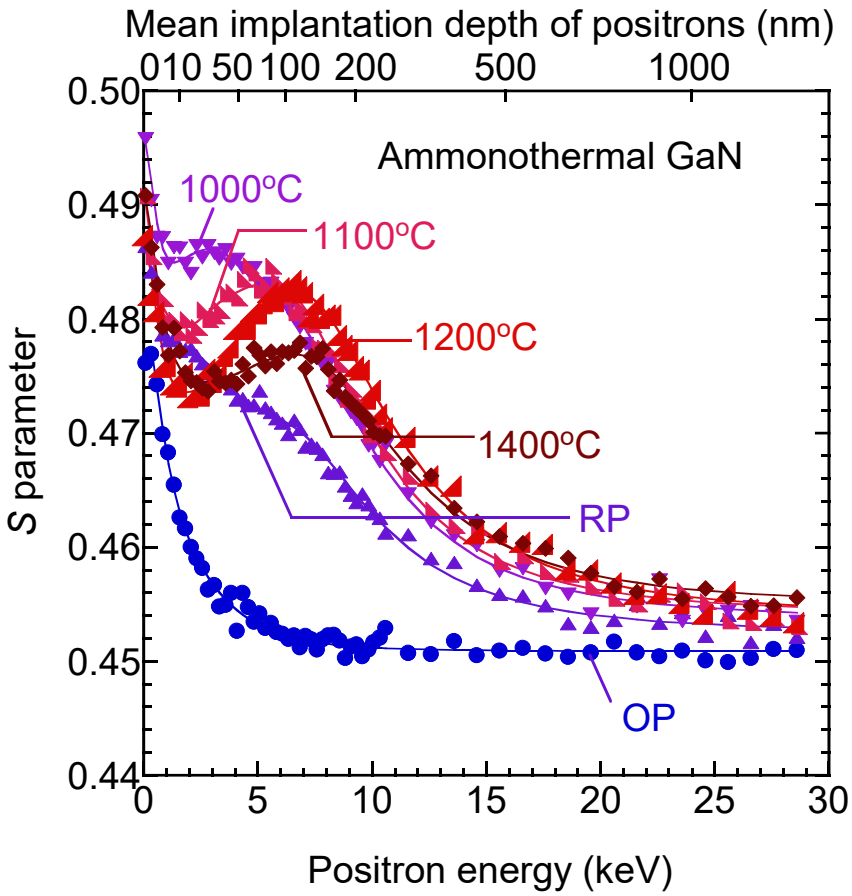
Mean implantation depth of positrons (nm)
0 10 50 100 200 500 1000
Ammonothermal GaN
1000°C
1100°C
1200°C
1400°C
RP
OP
S parameter
Positron energy (keV)
0.50
0.49
0.48
0.47
0.46
0.45
0.44
0
5
10
15
20
25
30

Fig. 3

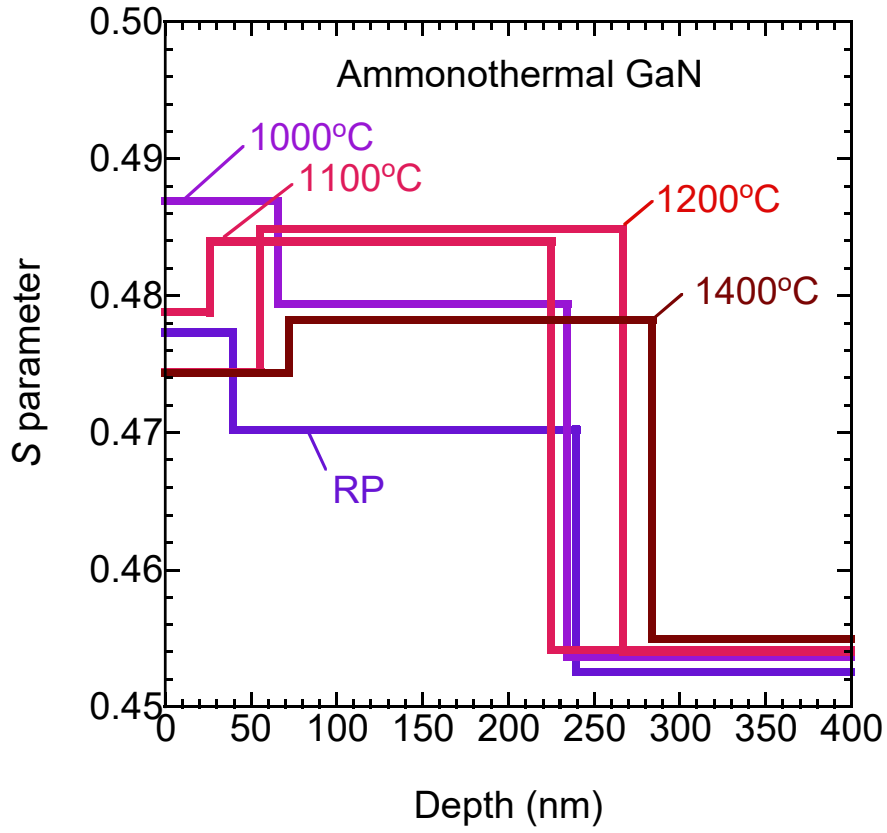
Ammonothermal GaN
1000°C
1100°C
1200°C
1400°C
RP
S parameter
Depth (nm)
0.50
0.49
0.48
0.47
0.46
0.45
0
50
100
150
200
250
300
350
400

Fig. 4

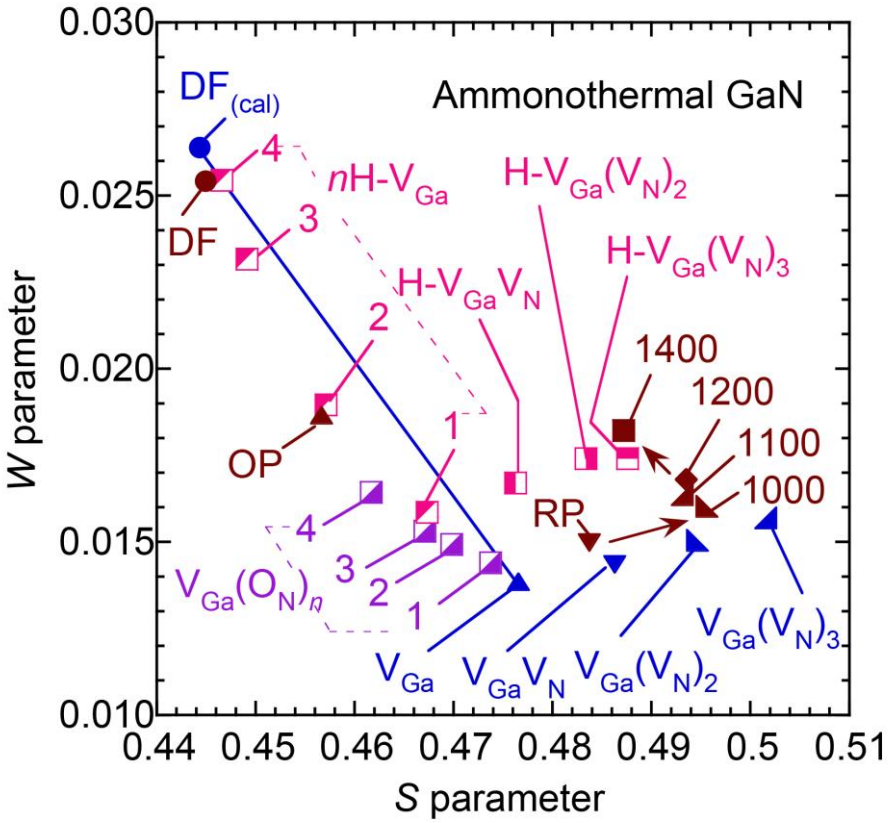
Ammonothermal GaN
DF(cal)
DF
4
3
2
1
nH-VGa
H-VGaVN
H-VGa(VN)2
H-VGa(VN)3
1400
1200
1100
1000
OP
RP
VGa(ON)n
VGa
VGaVN
VGa(VN)2
VGa(VN)3
W parameter
S parameter
0.030
0.025
0.020
0.015
0.010
0.44
0.45
0.46
0.47
0.48
0.49
0.5
0.51

Fig. 5

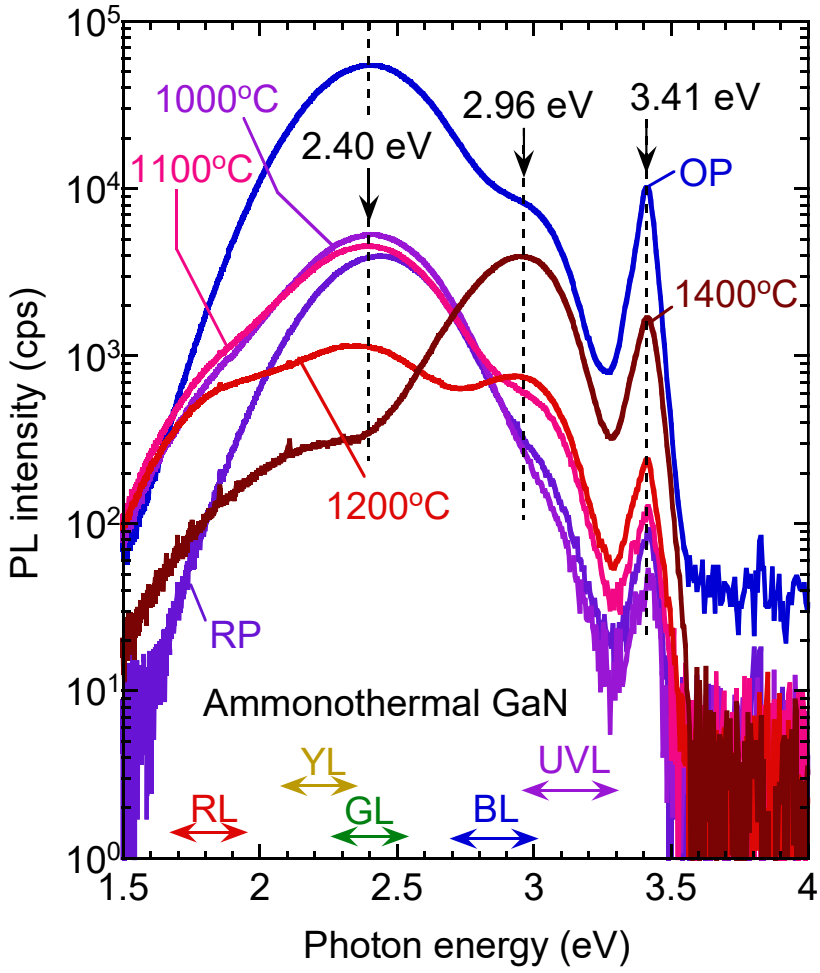
PL intensity (cps)
Photon energy (eV)
1000°C
1100°C
1200°C
1400°C
2.40 eV
2.96 eV
3.41 eV
OP
RP
Ammonothermal GaN
YL
RL
GL
BL
UVL

Fig. 6